Kobe University Repository : Kernel

PDF issue: 2025-12-05

Photocarrier transport dynamics in InAs/GaAs quantum dot superlattice solar cells using time-of-flight spectroscopy

Tanibuchi, T. ; Kada, T. ; Asahi, S. ; Watanabe, D. ; Kaizu, T. ; Harada, Y. ; Kita, T.

(Citation)
Physical Review B,94(19):195313-195313

(Issue Date)
2016-11-28

(Resource Type)
journal article

(Version)
Version of Record

(Rights)
©2017 American Physical Society

(URL)
https://hdl.handle.net/20.500.14094/90004054

KOBE UNIVERSITY

Photocarrier transport dynamics in InAs/GaAs quantum dot superlattice solar cells using time-of-flight spectroscopy

T. Tanibuchi, T. Kada, S. Asahi, D. Watanabe, T. Kaizu, Y. Harada, and T. Kita
Department of Electrical and Electronic Engineering, Graduate School of Engineering, Kobe University, 1-1 Rokkodai, Nada, Kobe 657-8501, Japan

(Received 18 February 2016; revised manuscript received 8 November 2016; published 28 November 2016)

We studied time-resolved photocarrier transport through InAs/GaAs quantum dot superlattice (QDSL) solar cells (SCs) using time-of-flight spectroscopy with an optical probe QD structure beneath the QDSL. Carriers optically pumped in the top *p*-GaAs layer were transported through the intrinsic layer, including the QDSLs, before arriving at the probe QDs. The photoexcited carrier density significantly influenced the time-resolved photoluminescence (PL) of the QDSLs and probe QDs. The time-resolved PL profile of the probe QDs indicated that excitation densities in excess of $25\mathrm{nJ/cm^2}$ drastically decreased the rise time, suggesting rapid carrier transport through the QDSLs. This was also confirmed by QDSL carrier transport dynamics, for which the PL intensity of the excited states decayed rapidly above this excitation power density, $25\mathrm{nJ/cm^2}$, while the ground state remained constant. These results demonstrate that filling the ground states of QDSLs and starting to populate the excited state miniband accelerates carrier transport in QDSL SCs. Furthermore, according to two-step photon absorption measurements taken with a 1.3-μm infrared laser light source, electrons play a key role in the generation of extra photocurrent by sub-band-gap photon irradiation.

DOI: 10.1103/PhysRevB.94.195313

I. INTRODUCTION

The next generation of high-conversion-efficiency solar cells (SCs) [1], e.g., multijunction [2,3], intermediate band (IB) [4–7], hot-carrier [8,9], and multiexciton generation SCs [10,11] have been proposed for breaking through the absolute conversion limit that is currently dominated by transmission and thermalization of incident photon energy [12]. The maximum conversion-efficiency limit, the so-called Shockley-Queisser limit, is estimated to be approximately 30% under one-sun illumination and approximately 40% under the maximum concentration of solar irradiance [13]. However, the theoretical maximum conversion efficiency of IBSCs can be as much as 48% under one-sun illumination [14]. IBSCs enable optical upconversion, which is caused by two-step photon absorption, i.e., cascade photoexcitation from the valence band to the conduction band by way of the IB, which leads to a reduction in the transmission loss of SCs [5,6].

The application of low-dimensional structures to semiconductor SCs has garnered much attention because of its suitability for harnessing photon energy from the sun [4,6]. Zero-dimensional quantum dots (QDs) spatially confine carriers in all directions. This confinement state can be regarded as part of the IB of the host semiconductor's band gap [4,6]. Furthermore, when QDs are vertically stacked closely enough to produce electronic coupling between adjacent QDs, QD superlattices (QDSLs) are formed, and minibands appear in the band gap [15]. Carriers can transport through the miniband, and photoexcited electrons and holes are accelerated away from each other in an internal electric field. This separation of electron and hole pairs in QDSLs increases carrier lifetime, thereby decreasing the recombination rate [16]. Obviously, carriers in the IB with longer lifetimes have greater potential for two-step photon absorption because the oscillator strength of the second photon absorption is proportional to the electron density in the IB [17]. Since carriers that are photoexcited and extracted from SCs contribute directly to the generation of electricity under operation of photovoltaics, these effects of QDSLs are very promising for realizing IBSCs.

Recently, we demonstrated that miniband formation in InAs/GaAs QDSL SCs increases extra photocarrier generation and improves the external quantum efficiency in the sub-band-gap region [17]. Conversely, carriers that are directly excited in the conduction band are easily trapped into the IB, reducing external quantum efficiency in the above-band-gap region. Overcoming this issue requires detailed understanding and precise control of dynamics for carriers transporting through QDSLs, specifically, dynamics that are limited by complicated trap and detrap processes. Various measurements such as photoluminescence (PL), time-resolved PL, and external quantum efficiency have been taken from photovoltaic devices of the same QDSL as the one used in this work [16,17]. However, these methods are not direct ways of observing carrier transport, as the signals contain complex information about carrier dynamics. In this case, the combined analysis of the information in various microscopic regions which are spatially separated is highly conducive to the clarification of the carrier transport dynamics in the QDSL SCs in terms of time scale. Recently, Toprasertpong *et al.* reported carrier time-of-flight measurements that had been taken with a probe structure inserted into the intrinsic layer of multiple-quantum-well SCs, in which they evaluated the carrier mobility in the multiple-quantum wells [18–20]. This technique is useful for studying ultrafast carrier transport dynamics on the subnanosecond scale. In this work, we have focused on carrier transport dynamics in InAs/GaAs QDSL SCs, as well as state-filling effects in QDSLs during carrier trapping and detrapping processes, using time-of-flight spectroscopy with an optical probe structure. We investigated the excitation power dependence of time-resolved PL of QDSLs and probe QDs and found that there is a critical excitation power density at which the carrier transport across the QDSLs is accelerated.

 ©2016 American Physical Society

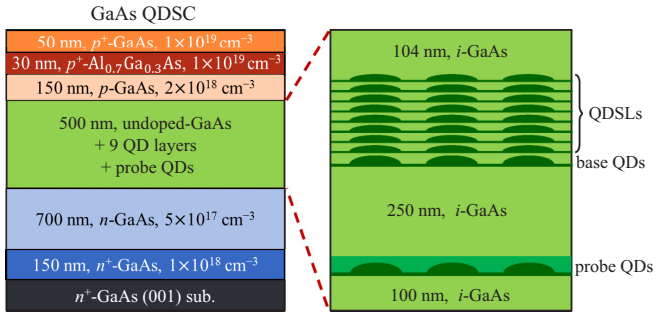

FIG. 1. Schematic diagram of the sample structure used in our time-of-flight measurement, GaAs QDSL-SC with probe QDs. Detailed structure in the undoped GaAs is shown on the right-hand side. The nine-layer-stacked InAs/GaAs QDs and InAs QDs capped by a strain reducing InGaAs layer were inserted into the intrinsic region.

II. QDSL SC STRUCTURE AND EXPERIMENTAL DETAILS

Figure 1 is a schematic diagram showing the structure of the QDSL SC sample used for the time-of-flight measurement. An InAs/GaAs QDSL-SC with a probe structure was grown on an n^+-GaAs (001) substrate by solid-source molecular beam epitaxy. The probe structure consisted of InAs QDs (probe QDs) capped with a 4-nm-thick $In_{0.2}Ga_{0.8}As$ layer that was grown at 430 °C, which was deposited on a buffer layer of i-GaAs(100 nm)/n-GaAs(700 nm)/n^+-GaAs(150 nm) that had been grown at 550 °C. The probe QDs were designed to have a different PL emission wavelength (1190 nm at 17 K) [21,22] than that of the QDSLs (1050 nm at 17 K) so that the spectrum could be resolved easily. After depositing a 10-nm i-GaAs layer that had been grown at 430 °C on top of the probe layer, followed by a 240-nm i-GaAs layer grown at 500 °C, eight-period InAs/GaAs QDSLs on base InAs QDs were grown at 480 °C. The total number of layers is nine. For the first QD layer, the base QDs, the nominal thickness of InAs was 2.0 monolayers. Each of the subsequent eight QD layers was 1.4 monolayers thick [15]. The GaAs-spacer-layer thickness of the stacked QDs was 4.0 nm so that they could be stacked closely enough to maintain coupling between the electronic states of the QDSLs along the direction of growth [15]. Afterwards, p^+-GaAs(50 nm)/p-AlGaAs(30 nm)/p-GaAs (150 nm)/i-GaAs(104 nm) layers were deposited on the QDSLs. The growth was performed in an As_2-flux environment, at a beam-equivalent pressure of 1.33×10^{-3} Pa. By design, the internal electric field strength was 28 kV/cm [16]. The sample was measured under short circuit condition to prevent alteration of the internal electric field by photoexcited carriers.

Continuous-wave PL was measured at 17 K to confirm the validity of the sample's spectral resolution. A laser diode with a 659-nm wavelength was used as the excitation light source. The PL signal was dispersed by a 30-cm single monochromator and detected by a liquid-nitrogen-cooled InGaAs-diode array.

Time-resolved PL was performed at 4 K with a near-infrared (IR) streak-camera system having a temporal resolution of approximately 20 ps. It is noted that, at temperatures less than approximately 20 K, the miniband does not form in the ground state (GS) of the QDSLs. When the energy states of the stacked QDs inhomogeneously distribute within the homogeneous energy width, they can be coupled to each other and form the miniband [15]. A typical homogeneous broadening of the GS has been reported to be less than 0.1 meV at low temperature [23], which is extremely smaller than the inhomogeneous broadening of approximately 35 meV. Therefore, complete electronic coupling over the eight stacked QDs hardly occurs at the low temperature and, therefore, the GS miniband is not formed. The GS miniband starts to form if temperature rises above ∼40 K [15]. Conversely, the homogeneous linewidth of the excited state (ES) is more than one order of magnitude larger than that of the GS [24]. Therefore, the ES easily results in miniband formation, even at low temperatures [17]. The excitation light used in our time-of-flight measurements was a pulse laser with a wavelength of 420 nm and a repetition rate of 80 MHz. The laser-spot diameter was 0.4 mm. The source of the pulse-light generation was a mode-locked Ti:sapphire pulse laser with a wavelength of 840 nm. A beta barium borate crystal was used to generate the second harmonic wavelength of the original light source, providing the excitation wavelength of 420 nm. Time of flight under IR irradiation was measured with a continuous-wave IR laser-light source (1300 nm) with a spot diameter of approximately 0.1 mm.

Figure 2 illustrates schematically the carrier transport dynamics in QDSL SCs that have a probe structure: (i) Carriers are selectively excited only in the top p-GaAs layer, according to both the thickness of the p-GaAs layer (150 nm) and the penetration depth of the excitation wavelength (approximately 30 nm). (ii) After photoexcited carriers reach the intrinsic region by diffusion, electrons are driven by the internal electric field and then arrive at the QDSLs, where they are repeatedly

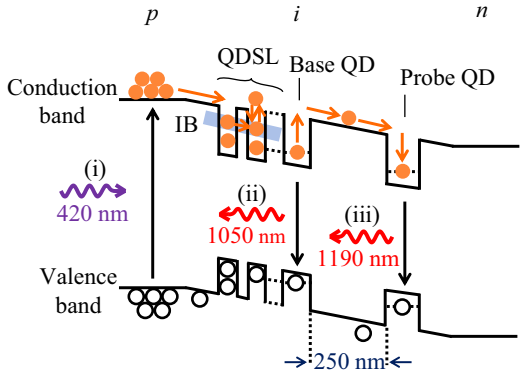

FIG. 2. Carrier transport dynamics in QDSL SCs that have a probe structure. The main three steps of our time-of-flight measurement are (i) carriers are selectively excited only in the top p-GaAs layer according to both the thickness of the p-GaAs layer (150 nm) and the penetration depth of the excitation wavelength (approximately 30 nm). (ii) After photoexcited carriers reach the intrinsic region by diffusion, electrons are driven by the internal electric field and then arrive at the QDSLs, where they are repeatedly trapped and detrapped. Holes also penetrate towards the n side by diffusion. A portion of the carriers recombine in the QDSLs. (iii) Other carriers can escape from the QDSL region and reach the probe QDs, where they recombine and emit photons.

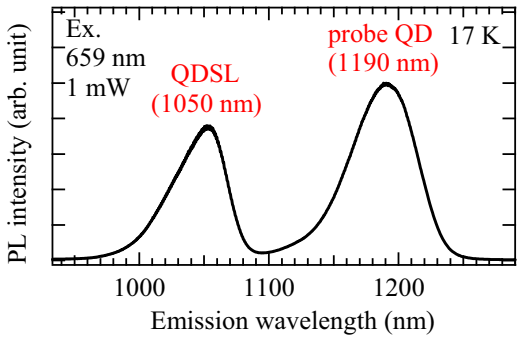

FIG. 3. PL spectrum of a QDSL SC with probe QDs at 17 K. QDSLs and probe QDs have peak emission wavelengths of 1050 and 1190 nm, respectively.

trapped and detrapped. Holes also penetrate towards the *n* side by diffusion. The portions of the carriers recombine in the QDSLs. (iii) Other carriers can escape from the QDSL region and reach the probe QDs, where they would recombine and emit photons.

By comparing the emission signals from the QDSLs and the probe QDs, carrier transport dynamics in the QDSLs can be analyzed precisely. First, the time-resolved PL profile of the probe QDs enables us to evaluate carrier transport time through the QDSLs. Second, the emission intensity of the probe QDs directly reflects the density of carriers that pass through the QDSLs and reach the probe QDs. Third, the temporal PL spectrum of the QDSLs shows the carrier transport dynamics inside the QDSLs.

III. RESULTS AND DISCUSSION

A. Time-of-flight spectroscopy of probe QDs

Figure 3 shows the PL spectrum of a QDSL SC with probe QDs measured at 17 K. QDSLs and probe QDs have peak emission wavelengths of 1050 and 1190 nm, respectively. Their wavelengths are designed to be spectrally resolved for time-of-flight measurement. The PL intensity of probe QDs is stronger than that of QDSLs at 1 mW. This is because the InGaAs cap on probe QDs serves as an effective carrier collection site.

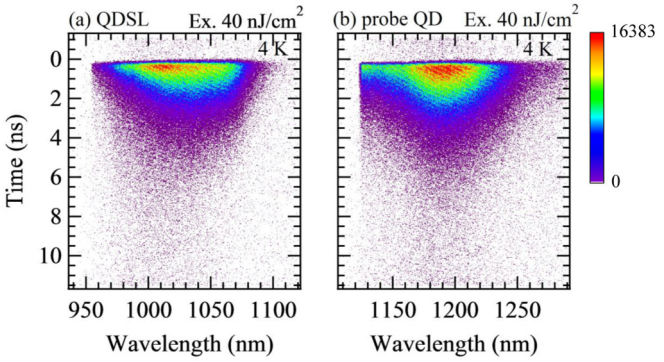

FIG. 4. Typical streak-camera images of (a) QDSLs and (b) probe QDs with excitation power density of 40 nJ/cm^2 at 4 K.

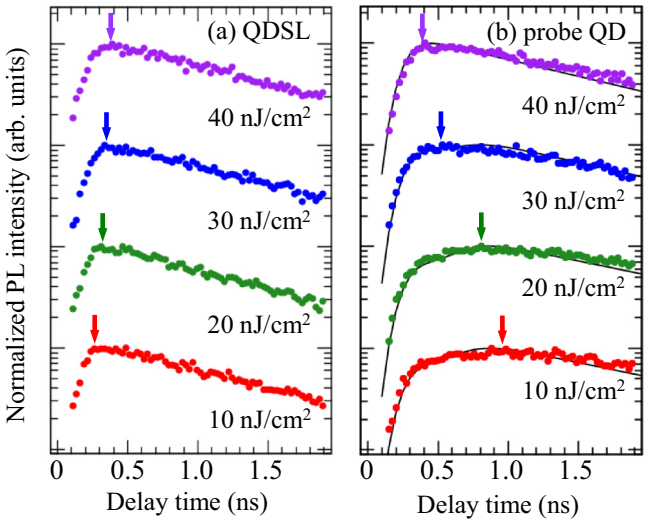

FIG. 5. Time-resolved PL profiles of (a) QDSLs and (b) probe QDs at various excitation power densities at 4 K. The zero delay time corresponds to the threshold of the increase in the QDSLs' PL intensity. The time-resolved PL profiles were recorded to within $\lambda_0 \pm 3$ nm of the time-resolved PL spectrum, where λ_0 is the peak PL wavelength of the signal, and the time scale for magnification ranges from 0 to 2.0 ns. The arrows in both figures at each excitation power density indicate the time at which PL begins to decay. Solid lines in Fig. 5(b) indicate simulated results based on a model taking into account diffusion current and drift current for electrons and holes influenced by multiple trap and detrap processes in QDSLs.

Figures 4(a) and 4(b) show typical streak-camera images of QDSLs and probe QDs at 4K. The injected excitation power density per pulse was 40nJ/cm^2. We proceed with the observation by analyzing these streak-camera images obtained by time-resolved PL at different excitation power densities.

Figures 5(a) and 5(b) show the time-resolved PL profiles of QDSLs and probe QDs with various excitation densities at 4 K. The zero delay time corresponds to the threshold of the increase in the QDSLs' PL intensity. At this temperature, all thermal effects are negligible. The time-resolved PL profiles were recorded to within $\lambda_0 \pm 3$ nm of the streak-camera image, where λ_0 is the peak PL wavelength of the signal, and the time scale for magnification ranges from 0 to 2.0 ns. As can be seen in Fig. 5(a), the time-resolved PL profile of the QDSLs differs only slightly with respect to excitation power density, while that of probe QDs changes with increasing excitation power density (indicated by the arrows). The slight change in the peak PL time of QDSLs is due to a thermalization process that occurs in the nonresonant excitation with some excess energy [25]. Conversely, in the case of probe QDs, by increasing the excitation power density from 10 to 40nJ/cm^2, the time at which the PL begins to decay, indicated by the arrow in Fig. 5(b), decreases dramatically. The excitation power density dependence of the delay time indicating the maximum of a hump developed in the decay curves of probe QDs is shown in Fig. 6(a). Before reaching the excitation power density of 25nJ/cm^2, the time delay is pronounced, suggesting that carriers arrive later. Further increase in the excitation power density causes a quick rise in the PL intensity. This implies that

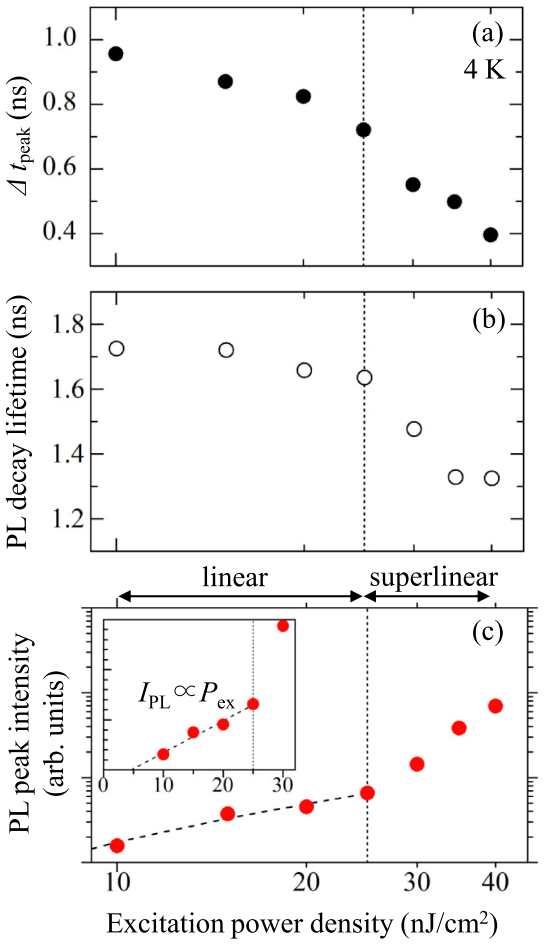

FIG. 6. Excitation power density dependences of (a) delay time indicating the maximum of a hump developed in the decay curves, (b) PL decay lifetime, and (c) PL peak intensity for probe QDs at 4 K. The dotted lines represent the critical point. The scales of both axes in (c) are logarithmic. The low- and high-excitation regions have linear and superlinear slopes, respectively. The dashed line is a linear plot for a guide to the eye. The inset figure shows the linear relationship of the excitation power density dependence.

a sort of triggering effect occurs in carrier transport dynamics. Such carrier transport dynamics has also influenced the PL decay time of the probe QDs. As summarized in Fig. 6(b), the PL decay time measured at the weak excitation power density was approximately 1.7 ns, which slightly decreases with increasing the excitation power density up to 25 nJ/cm^2. This slow PL decay is caused by carriers arriving later. The decay time drastically decreases when excited above the critical point and approaches a typical intrinsic value of approximately 1 ns for single InAs QDs. One straightforward assumption of the triggering effect is that rapid carrier flow across the QDSL layer results in many more carriers reaching the probe QDs in less time. This rapid carrier flow would be caused by the generation of a large number of carriers of high-excitation power density filling the quantum states of the QDSLs. After these states begin to fill with carriers that arrive sooner, later carriers have a lower probability of trapping into QDSLs, due to Pauli blocking. This results in rapid carrier arrival at the probe QDs. Next, we examine the carrier transport dynamics in detail.

Figure 6(c) shows the excitation power density dependence of the peak PL intensity for the probe QDs at 4 K. The scale of both axes is logarithmic. Since PL intensity directly reflects the number of carriers, a PL intensity of 10 nJ/cm^2 indicates that fewer carriers of low-excitation power density have reached the probe QDs. We note that there is a critical point in Fig. 6; the plot can be divided into two regions representing linear and superlinear slopes. In the low-excitation region, the relationship between excitation power density and peak PL intensity is almost linear. As shown in the inset of Fig. 6(c), there is a threshold for the PL peak intensity of probe QDs. The threshold excitation power density was approximately 5 nJ/cm^2. This excitation power density corresponds to the carrier density of 1.05×10^{10} cm^{-2}, which coincides roughly with the in-plane QD density of approximately 1.0×10^{10} cm^{-2}. The threshold excitation power density corresponds to an initial carrier consumption in QDSLs. The relationship becomes superlinear in the high-excitation region. In addition, the coincidence of the critical point in Fig. 6 assures the existence of a triggering effect at 25 nJ/cm^2. This drastic change in the relationship between excitation power density and PL intensity can be understood by careful observation of how the carriers behave in this system. The electrons are accelerated towards the n layer by the electric field and transported through the QDSLs, after which they arrive at the probe QDs. In contrast, the holes are accelerated in the direction of the surface by the internal electric field. Carrier diffusion causes some of the holes to move towards the QDSLs. Thus, the transport of the hole is considered to limit the dynamics in probe QDs. To clarify the effects of carrier transfer on the temporal evolution of PL from the probe QDs in Fig. 5, we conducted a theoretical calculation based on carrier dynamics in the p-i-n SC structure. Here we took into account one-dimensional diffusion current and drift current for electrons and holes influenced by multiple trap and detrap processes in QDSLs. These are given by

$$\frac{\partial n(t,x)}{\partial t} = -\mu_e E \frac{\partial n(t,x)}{\partial x} + D_e \frac{\partial^2 n(t,x)}{\partial x^2}, \quad (1)$$

$$\frac{\partial p(t,x)}{\partial t} = \mu_h E \frac{\partial p(t,x)}{\partial x} + D_h \frac{\partial^2 p(t,x)}{\partial x^2}, \quad (2)$$

where $n(t,x)$ and $p(t,x)$ are electron and hole densities at a time t and a position x, E is the electric field, and μ_e (μ_h) and D_e (D_h) are the effective mobility and diffusion constant of the electron (hole), respectively. Here we used a bulk approximation taking into account trap and detrap processes in the mobility. The diffusion constant is given by the Einstein relation with the mobility. Furthermore, we dealt with a thermal carrier escape rate from QDSLs, which is proportional to $e^{-t/\tau_{\text{thermal}}}$. We assumed that all carriers arriving at probe QDs are completely collected and radiatively recombine according to

$$I(t) \propto \int_0^t n(t',x_{\text{probe}}) p(t',x_{\text{probe}}) \exp\left(-\frac{t-t'}{\tau_r}\right) dt', \quad (3)$$

where x_{probe} is the position of the probe QD layer and τ_r is the recombination lifetime shown in Fig. 6(b). Solid lines added in Fig. 5(b) indicate calculated results of $I(t)$, reproducing well the experimental curves. Here we used two sets of parameters

TABLE I. Fitting parameters used in theoretical simulations of time-resolved PL profiles in Fig. 5.

	Slow component	Fast component
μ_h (cm^2/Vs)	0.11	0.19
μ_e (cm^2/Vs)	2.4	4.1
$\tau_{thermal}$ (ns)	0.13	0.07

representing features of a slow transport in the linear region and a relatively fast transport in the superlinear region. The fitted parameters are summarized in Table I.

We used the hole mobility of $0.11\,cm^2/s$ based on the carrier velocity estimated from the difference between two time-resolved PL profiles of the GS transition in the base QDs obtained at weak and strong excitation power densities. At the strong excitation power density, the carriers can arrive at the base QDs through the 32-nm QDSL region. Its delayed time was approximately 1 ns, which corresponds to an average carrier velocity of 3200 cm/s. When this carrier velocity is divided by the internal electric field of 28 kV/cm, the hole mobility can be roughly derived to be $0.11 cm^2/Vs$. Detailed time-resolved PL profiles are shown in Fig. 9 and the evaluated result of the hole mobility is discussed later. We roughly assumed the ratio of the electron and hole mobilities is the same as that of bulk GaAs. The estimated hole mobility is on the same order of magnitude as that which is derived from the time-of-flight measurement of multiple-quantum-well SCs [19], where carriers inevitably pass through the quantum structure to arrive at the probe layer. According to the calculations, the temporal evolution of the probe QD PL is limited by hole transport and delayed carrier transport caused by multiple trap and detrap processes in QDSLs gives rise to the slow rise profile significantly observed in the lower-excitation power density. The time-resolved PL profiles in the linear region were reproduced by a superposition of the slow and fast components. The ratio of the fast (slow) component at 10 and $20\,nJ/cm^2$ is 0.55 (0.45). The fast and slow decay components can be attributed to carriers transporting through areas without and with QDSLs, respectively. Conversely, with increasing the excitation power density, the delayed process is suppressed by a state filling in QDSLs. In the superlinear region, the fast component becomes dominant with increasing the excitation power density. The fast component increases to 0.7 at $30\,nJ/cm^2$ and, eventually, the profile at $40\,nJ/cm^2$ obeys a relation given by the only fast component. The estimated time constant of thermal carrier escape becomes short with increasing the excitation power density. This is caused by a rise of the quasi-Fermi level. As the number of the injected carriers increases with increasing excitation power density, the GS of the QDSLs begin to fill, and population of the ES miniband accelerates carrier transport in the QDSLs. Hence the density of electrons and holes that pass through the QDSLs increases dramatically. The result in the superlinear region suggests that the increasing rate is caused by nonlinear carrier supply to probe QDs because the band profile in the event center, QDSLs that work as the bottleneck for carrier transport, becomes renormalized when QDSL states are filled [26].

When we simply compare the total density of the GS of eight-period QDSLs and base QDs with the carrier density excited by a single pulse of $10-40\,nJ/cm^2$, the carrier density is smaller than the GS density of $1.8 \times 10^{11} cm^{-2}$ even at $40 nJ/cm^2$ corresponding to $8.4 \times 10^{10} cm^{-2}$. The time-resolved PL profile of probe QDs at $40\,nJ/cm^2$ obeys a relation given by the only fast rise component with the properties listed in Table I. This fast component arises from a quick transport through the ES minibands. The excited carrier density smaller than the total GS density of QDSLs and base QDs suggests that the quick transport occurs even if the GSs are not completely filled. Such carrier transport through the ES miniband of the QDSLs without relaxation to unfilled GSs has been observed in our previous time-resolved PL measurements for the GS transition of QDSLs under various internal electric fields [17]. Here we have confirmed an extended decay component arising from spatial carrier separation in the ES miniband. The carrier transport in the ES miniband is driven by the internal electric field. This happens even if the GSs are not completely filled. Above the critical excitation power density of $30\,nJ/cm^2$, the fast component starts increasing, which means that carrier transport through the ES miniband begins to occur when carriers of $6.3 \times 10^{10} cm^{-2}$ corresponding to $30\,nJ/cm^2$ are supplied.

B. Carrier transport dynamics in QDSLs

Figure 7(a) shows the excitation-power-dependent PL spectrum of QDSLs. In our earlier work regarding PL properties of QDSLs with various stacking layer numbers [15], we distinguished PL signals from the QDSL region consisting of 1.4-monolayer InAs, with 2.0-monolayer InAs QDs forming the base. The PL peak appearing at 1060 nm is attributed to the GS of the base QDs, which is labeled GS (base QDs). Due to the large size of the base QDs, their electronic state is isolated from that of the QDSLs that are formed above the base QDs. The GS signal of the QDSLs is indicated by the arrow labeled GS (QDSLs) at 1030 nm. Carrier population increases with increasing excitation power, and then the ES signal of the QDSLs begins to dominate, as indicated by the arrow labeled by ES (QDSLs) at 980 nm. Time-resolved carrier population in QDSLs was observed. Figure 7(b) shows the time-integrated PL spectra of QDSLs, measured at excitation densities of $10\,nJ/cm^2$ (red line) and $40\,nJ/cm^2$ (purple line) at 4 K. The PL spectra were obtained by time-integrating the streak-camera image by 0.5 ns, from 0 to 2.0 ns. The spectra at $10\,nJ/cm^2$ are almost independent of the time delay, although the spectra at $40\,nJ/cm^2$ vary with changing carrier population in the energy states of ES (QDSLs), GS (QDSLs), and GS (base QDs). Just after the strong pulse excitation of $40\,nJ/cm^2$, excited carriers fill the GS (QDSLs) and GS (base QDs) and are populated in the ES (QDSLs), as shown by the spectrum integrated between 0 and 0.5 ns. It is noted that the ES (QDSLs) signal at 980 nm weakens with the time delay. Conversely, the GS (QDSLs) signal at 1030 nm increases slightly, and the GS (base QDs) signal at 1060 nm also gradually increases with the time delay. These temporal evolutions indicate that populated carriers relax from ES (QDSLs) towards GS (QDSLs) and GS (base QDs).

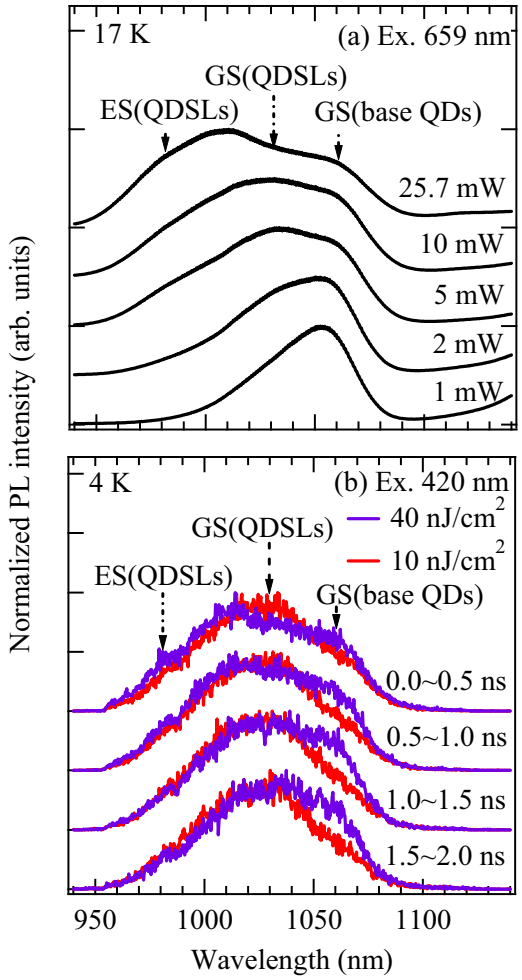

FIG. 7. (a) The excitation-power-dependent PL spectrum of QDSLs. The GS signal of the QDSLs is indicated by the arrow labeled GS (QDSLs) at 1030 nm. The signal appearing at 1060 nm is attributed to the GS of the base QDs, which is labeled GS (base QDs). Carrier population increases with increasing excitation power, and then the ES signal of the QDSLs begins to dominate, as indicated by the arrow labeled "ES (QDSLs)" at 980 nm. (b) Time-resolved PL spectra of QDSLs, measured at excitation power densities of 10 nJ/cm^2 (red line) and 40 nJ/cm^2 (purple line) at 4 K. The PL spectra were obtained by time-integrating the streak-camera image by 0.5 ns, from 0 to 2.0 ns.

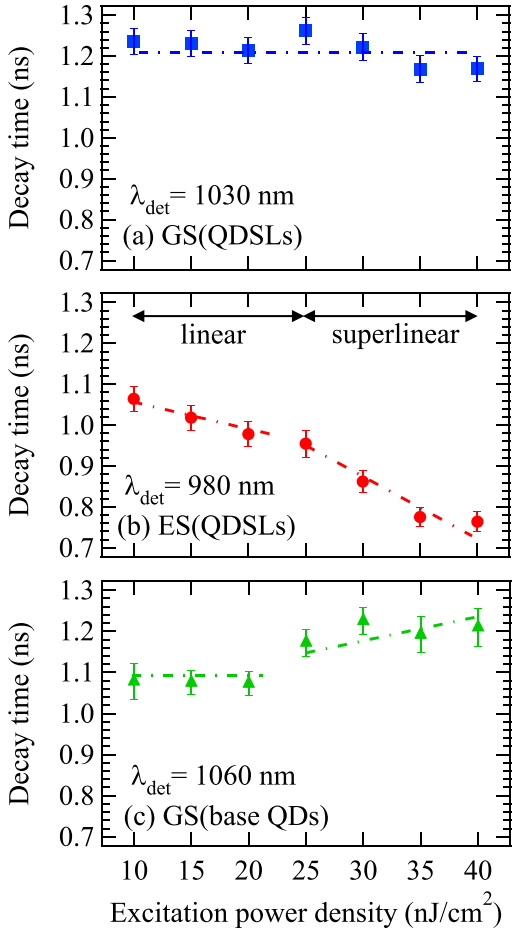

FIG. 8. PL decay times that were analyzed for (a) GS (QDSLs) at 1030 nm, (b) ES (QDSLs) at 980 nm, and (c) GS (base QDs) at 1060 nm.

Next, we studied detailed time-resolved PL as a function of excitation power density. Figure 8 summarizes the results of PL decay times that were analyzed for (a) GS (QDSLs) at 1030 nm, (b) ES (QDSLs) at 980 nm, and (c) GS (base QDs) at 1060 nm. In Fig. 8(a), the result for GS (QDSLs) indicates a stable decay time of approximately 1.2 ns at any excitation power density. Figure 8(b) shows the decay time of the ES (QDSLs). Due to an inhomogeneous distribution of QDSLs, the shorter-wavelength side of the inhomogeneous PL signal from the GS (QDSLs) is also detected at the wavelength of the ES (QDSLs). Thereby, at a weak excitation condition of 10 nJ/cm^2, the decay time approximates that of the GS (QDSLs), at which the ES (QDSLs) does not appear clearly. With increasing the excitation power density up to approximately 25 nJ/cm^2, the ES (QDSLs) component showing a rapid decay caused by energy relaxation into the GS gradually starts increasing. While filling the GS (QDSLs), the contribution of the ES (QDSLs) PL gradually increases. As the excitation power density continues to increase beyond approximately 25 nJ/cm^2, the PL from the ES (QDSLs) decays much faster because carrier transport in the ES miniband of QDSLs becomes dominant. Conversely, the decay time of the GS (base QDs) PL increases beyond approximately 25 nJ/cm^2, which indicates that carriers arrive at the base QDs later. These critical points coincide with the ones observed in the results shown in Figs. 5(b) and 6. Hence Figs. 8(a)–8(c) also illustrate the evidence that rapid carrier penetration towards the *n*-layer side is caused by the state filling that results from high-excitation power density.

Figure 9(a) compares the time-resolved PL profiles detected at the GS (base QDs) transitions at 10 and 40nJ/cm^2. The time-resolved PL profile was integrated between 1060 and 1070 nm. The difference of the PL intensity between the two profiles is shown in Fig. 9(b). The strong excitation causes a slight delay in the PL rise process and, after the maximum intensity was achieved, the slower PL decay was observed at 40 nJ/cm^2. The delayed carriers arriving at the base QDs at 40 nJ/cm^2 are consistent with the results in Figs. 7 and 8. The PL-intensity difference reaches its peak at approximately

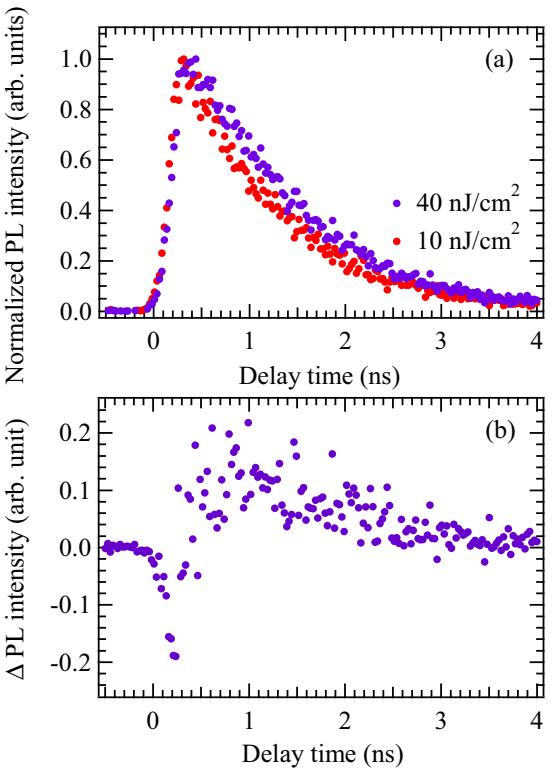

FIG. 9. (a) Time-resolved PL profiles detected at the GS (base QDs) transitions at 10 and 40 nJ/cm^2. The time-resolved PL profile was integrated between 1060 and 1070 nm. (b) The difference between the two profiles in Fig. 9(a).

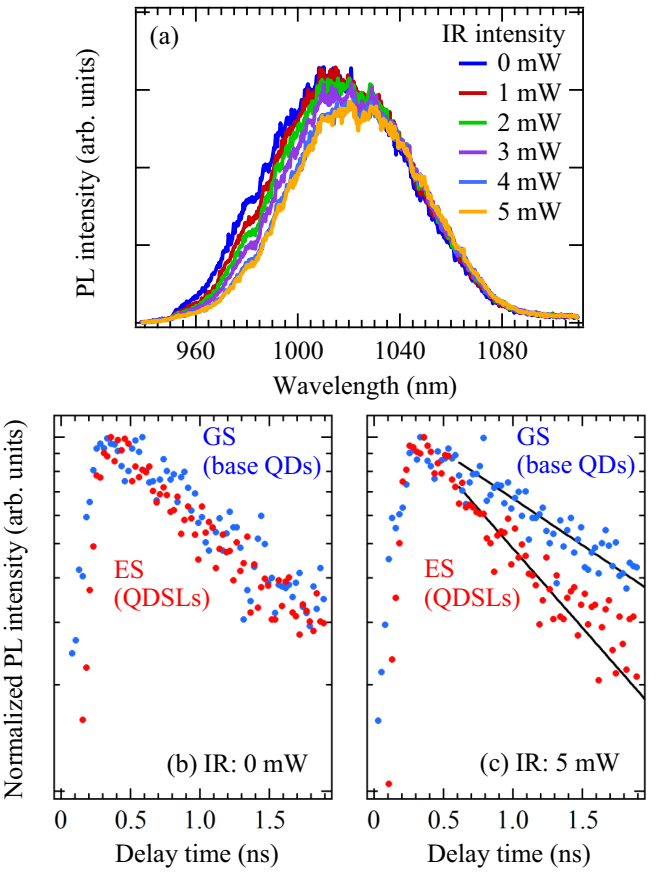

FIG. 10. (a) PL spectra of QDSLs at various IR powers. Time-resolved PL of QDSLs (b) without and (c) with IR irradiation, 5 mW, focusing on the ES (QDSLs) at 980 nm and the GS (base QDs) at 1060 nm. Solid lines indicate fitted single-exponential decay curves.

1 ns. This time scale can be regarded as necessary for carrier transport through a 32-nm QDSL region, which corresponds to an average carrier velocity of 3200 cm/s. As mentioned above, this carrier velocity is on the same order of magnitude as that which is derived from the time-of-flight measurement of multiple-quantum-well SCs [19]. According to the estimated carrier velocity and the internal electric field of 28 kV/cm, the mobility can be roughly derived to be 0.11cm^2/Vs.

Perpendicular transport across the SL structure, of course, depends on barrier thickness. Overlapping of the wave functions of carriers in the neighboring QDs causes broadening of the energy levels and forms minibands with dispersed states. Miniband formation of the ES plays a key role to improve carrier transport across QDSLs despite localization of the GS at 4 K. Besides, since the observation of PL implies a perpendicular motion of both electrons and holes, contribution of both the electron and hole minibands should be considered. According to Refs. [4,27], the one-dimensional miniband formation depends on, for example, strain distribution, QD shape, and composition gradation (potential gradation) caused by In segregation as well as barrier thickness. The miniband width in the conduction band dramatically increases when the barrier thickness is less than approximately 10 nm (see Ref. [4]). Similar things happen in the valence band, where the electronic states are very complicated because of state mixing in the one-dimensional SL structure as discussed in Refs. [15,27,28]. The miniband width in the valence band is expected to be smaller than the one in the conduction band at the same barrier thickness because of the difference in the effective mass. The degree of energy levels broadening into a miniband is different for electrons and holes and influences the carrier velocity. A smaller miniband width causes a smaller mobility (see Refs. [29,30]). The experimentally estimated averaged carrier velocity across QDSLs was very slow, which is comparable to the value (Fig. 4 in Ref. [19]) estimated for InGaAs/GaAsP multiquantum wells with a barrier thickness of 6.2 nm. The slow carrier velocity in QDSLs is considered to be preferentially limited by a relatively small hole miniband width.

C. Two-step photoexcitation process

Finally, the time-of-flight measurement under an additional IR irradiation was also taken with a continuous-wave IR (1300 nm) laser with 10nJ/cm^2 of 420-nm pulse excitation. Figure 10(a) shows PL spectra of QDSLs at various IR powers. The shorter-wavelength side of the PL spectrum is sliced according to the increase in IR irradiation, suggesting that the quasi-Fermi level decreases according to the accumulated carrier density in QDSLs. We also analyzed the time-resolved PL of QDSLs with and without IR irradiation, focusing on the ES (QDSLs) at 980 nm and the GS (base QDs) at 1060 nm. The time-resolved PL profiles from the streak-camera image are

displayed by wavelength in Figs. 10(b) and 10(c). Figure 10(b) shows that the time-resolved PL profiles measured without IR irradiation are almost the same as those shown in Fig. 8, while Fig. 10(c) illustrates an obvious difference between time-resolved PL profiles given the presence of IR irradiation. At 980 nm, decay with IR irradiation increases faster than without. Conversely, the decay time at 1060 nm becomes slower with IR irradiation. According to fitting the curves indicated in Fig. 10(c), the decay times at ES (QDSLs) are 1.13 and 0.97 ns for without and with IR irradiation, respectively. On the other hands, the decay times at GS (base QDs) are 1.24 and 1.65 ns for without and with IR irradiation, respectively. When we expose the QDSLs to IR radiation, the electrons in the GS (QDSLs) are pumped out towards the conduction band, and the electrons in the ES (QDSLs) quickly relax to the GS (QDSLs). Consequently, the PL intensity of the ES (QDSLs) decays rapidly. The excited electrons drift with the internal electric field and are supplied to base QDs, whose delayed carrier supply from QDSLs causes the slow PL decay of the GS (base QDs). On the other hand, if holes are dominantly excited by the IR laser, excited holes are going to drift towards the p side, so that the PL decay time of the GS (base QDs) becomes shorter than one without IR irradiation. These results prove that IR irradiation prompts excitation of electrons that have accumulated in the GS (QDSLs) [17] and inhibits the contribution of holes in the two-step photon absorption.

IV. SUMMARY

We have systematically studied time-resolved photocarrier transport through InAs/GaAs QDSL-SCs, using time-of-flight spectroscopy with an optical probe QD structure beneath the QDSL. Photoexcited carriers pumped in the top p-GaAs layer are transported through the intrinsic layer, including the QDSLs, and arrive at the probe QDs. The time-resolved profiles of QDSLs and probe QDs suggest a triggering effect in carrier transport dynamics. Above the excitation power density ($25\mathrm{nJ/cm^2}$), the time-resolved PL profile of probe QDs clearly decreases in rise time, reflecting rapid carrier transport across the QDSLs. We confirmed that this rapid carrier transport influences the carrier transport dynamics across the QDSLs. These results demonstrate that high-excitation power density leads to the state filling of the GS (QDSLs), which in turn leads to advantageous conditions for carrier transport in QDSL SCs. We estimated an averaged carrier velocity across the QDSL region according to the difference profile of PL-decay curves at different excitation densities. Furthermore, during two-step photon absorption measurements using a 1.3-μm IR laser light source, intraband electron excitation to the conduction band was clearly observed in terms of time scale. When we shone the IR light on the QDSLs, the electrons in the GS (QDSLs) were pumped out towards the conduction band, and electrons in the ES (QDSLs) quickly relaxed into the GS (QDSLs). According to these results, we have demonstrated the strong potential of time-of-flight measurement for studying the microscopic carrier transport dynamics in terms of time scale and, furthermore, optimizing the operation condition such as solar radiation density realizing an ideal IBSC operation.

ACKNOWLEDGMENTS

This work has been partially supported by the Incorporated Administrative Agency New Energy and Industrial Technology Development Organization (NEDO) and the Ministry of Economy, Trade, and Industry (METI), Japan. Also, this work was partially supported by JSPS KAKENHI Grant No. 15K13953. The authors would like to thank M. Sugiyama and K. Toprasertpong of the University of Tokyo for fruitful discussions about time-of-flight measurements.

[1] M. A. Green, Prog. Photovoltaics **9**, 123 (2001).
[2] A. De Vos, J. Phys. D: Appl. Phys. **13**, 839 (1980).
[3] N. J. Ekins-Daukes, J. M. Barnes, K. W. J. Barnham, J. P. Connolly, M. Mazzer, J. C. Clark, R. Grey, G. Hill, M. A. Pate, and J. S. Roberts, Sol. Energy Mater. Sol. Cells **68**, 71 (2001).
[4] S. Tomić, Phys. Rev. B **82**, 195321 (2010).
[5] A. Luque and A. Martí, Phys. Rev. Lett. **78**, 5014 (1997).
[6] A. Luque, A. Martí, and C. Stanley, Nat. Photonics **6**, 146 (2012).
[7] Y. Okada, T. Morioka, K. Yoshida, R. Oshima, Y. Syoji, T. Inoue, and T. Kita, J. Appl. Phys. **109**, 024301 (2011).
[8] D. Watanabe, N. Kasamatsu, Y. Harada, and T. Kita, Appl. Phys. Lett. **105**, 171904 (2014).
[9] R. T. Ross and A. J. Nozik, J. Appl. Phys. **53**, 3813 (1982).
[10] V. I. Klimov, Appl. Phys. Lett. **89**, 123118 (2006).
[11] O. E. Semonin, J. M. Luther, S. Choi, H. Chen, J. Gao, A. J. Nozik, and M. C. Beard, Science **334**, 1530 (2011).
[12] L. C. Hirst and N. J. Ekins-Daukes, Prog. Photovoltaics **19**, 286 (2011).
[13] W. Shockley and H. J. Queisser, J. Appl. Phys. **32**, 510 (1961).
[14] Y. Okada, N. J. Ekins-Daukes, T. Kita, R. Tamaki, M. Yoshida, A. Pusch, O. Hess, C. C. Phillips, D. J. Farrell, K. Yoshida, N. Ahsan, Y. Shoji, T. Sogabe, and J.-F. Guillemoles, Appl. Phys. Rev. **2**, 021302 (2015).
[15] A. Takahashi, T. Ueda, Y. Bessho, Y. Harada, T. Kita, E. Taguchi, and H. Yasuda, Phys. Rev. B **87**, 235323 (2013).
[16] N. Kasamatsu, T. Kada, A. Hasegawa, Y Harada, and T. Kita, J. Appl. Phys. **115**, 083510 (2014).
[17] T. Kada, S. Asahi, T. Kaizu, Y. Harada, T. Kita, R. Tamaki, Y. Okada, and K. Miyano, Phys. Rev. B **91**, 201303 (2015).
[18] K. Toprasertpong, N. Kasamatsu, H. Fujii, T. Kada, S. Asahi, Y. Wang, K. Watanabe, M. Sugiyama, T. Kita, and Y. Nakano, IEEE J. Photovolt. **4**, 1518 (2014).
[19] K. Toprasertpong, N. Kasamatsu, H. Fujii, T. Kada, S. Asahi, Y. Wang, K. Watanabe, M. Sugiyama, T. Kita, and Y. Nakano, Appl. Phys. Lett. **107**, 043901 (2015).

[20] K. Toprasertpong, T. Tanibuchi, H. Fujii, T. Kada, S. Asahi, K. Watanabe, M. Sugiyama, T. Kita, and Y. Nakano, IEEE J. Photovoltaics **5**, 1613 (2015).
[21] K. Nishi, H. Saito, S. Sugou, and J. S. Lee, Appl. Phys. Lett. **74**, 1111 (1999).
[22] N. Ozaki, T. Yasuda, S. Ohkouchi, E. Watanabe, N. Ikeda, Y. Sugimoto, and R. A. Hogg, Jpn. J. Appl. Phys. **53**, 04EG10 (2014).
[23] P. Borri, W. Langbein, S. Schneider, U. Woggon, R. L. Sellin, D. Ouyang, and D. Bimberg, Phys. Rev. Lett. **87**, 157401 (2001).
[24] S. Seidl, M. Kroner, C. Lux, A. W. Holleitner, K. Karrai, R. J. Warburton, A. Badolato, and P. M. Petroff, Appl. Phys. Lett. **92**, 153103 (2008).
[25] D. Oberhauser, K. H. Pantke, W. Langbein, V. G. Lyssenko, H. Kalt, J. M. Hvam, G. Weimann, and C. Klingshirn, Phys. Status Solidi B **173**, 53 (1992).
[26] K. Yoshida, Y. Okada, and N. Sano, J. Appl. Phys. **112**, 084510 (2012).
[27] M. Usman, T. Inoue, Y. Harda, G. Klimeck, and T. Kita, Phys. Rev. B **84**, 115321 (2011).
[28] Y. Ikeuchi, T. Inoue, M. Asada, Y. Harada, T. Kita, E. Taguchi, and H. Yasuda, Appl. Phys. Express **4**, 062001 (2011).
[29] B. Deveaud, J. Shah, T. C. Damen, B. Lambert, and A. Regreny, Phys. Rev. Lett. **58**, 2582 (1987).
[30] F. Capasso, K. Mohammed, and A. Y. Cho, IEEE J. Quantum Electron. **22**, 1853 (1986).